Low energy scattering cross section ratios of ^{14}N(p,p)^{14}N

R. J. deBoer,* D. W. Bardayan, J. Görres, P. J. LeBlanc, K. V. Manukyan, M. T. Moran, K. Smith,† W. Tan, E. Uberseder,‡ and M. Wiescher
The Joint Institute for Nuclear Astrophysics, Department of Physics, University of Notre Dame, Notre Dame, Indiana 46556, USA

P. F. Bertone§ and A. E. Champagne
Department of Physics, University of North Carolina at Chapel Hill, Chapel Hill, North Carolina 27599, USA and Triangle Universities Nuclear Laboratory, Durham, North Carolina 27708, USA

M. S. Islam
Department of Physics and Astronomy, Ball State University, Muncie, Indiana 47306, USA
(Received 17 January 2015; published 20 April 2015)

Background: The slowest reaction in the first CNO cycle is ^{14}N(p,γ)^{15}O, therefore its rate determines the overall energy production efficiency of the entire cycle. The cross section presents several strong resonance contributions, especially for the ground-state transition. Some of the properties of the corresponding levels in the ^{15}O compound nucleus remain uncertain, which affects the uncertainty in extrapolating the capture cross section to the low energy range of astrophysical interest.
Purpose: The ^{14}N(p,γ)^{15}O cross section can be described by using the phenomenological R matrix. Over the energy range of interest, only the proton and γ-ray channels are open. Since resonance capture makes significant contributions to the ^{14}N(p,γ)^{15}O cross section, resonant proton scattering data can be used to provide additional constraints on the R-matrix fit of the capture data.
Methods: A 4 MV KN Van de Graaff accelerator was used to bombard protons onto a windowless gas target containing enriched ^{14}N gas over the proton energy range from $E_p = 1.0$ to 3.0 MeV. Scattered protons were detected at $\theta_{\rm lab} = 90$, 120°, 135°, 150°, and 160° using ruggedized silicon detectors. In addition, a 10 MV FN Tandem Van de Graaff accelerator was used to accelerate protons onto a solid Adenine ($C_5H_5N_5$) target, of natural isotopic abundance, evaporated onto a thin self-supporting carbon backing, over the energy range from $E_p = 1.8$ to 4.0 MeV. Scattered protons were detected at 28 angles between $\theta_{\rm lab} = 30.4°$ and 167.7° by using silicon photodiode detectors.
Results: Relative cross sections were extracted from both measurements. While the relative cross sections do not provide as much constraint as absolute measurements, they greatly reduce the dependence of the data on otherwise significant systematic uncertainties, which are more difficult to quantify. The data are fit simultaneously using an R-matrix analysis and level energies and proton widths are extracted. Even with relative measurements, the statistics and large angular coverage of the measurements result in more confident values for the energies and proton widths of several levels; in particular, the broad resonance at $E_{\rm c.m.} = 2.21$ MeV, which corresponds to the $3/2^+$ level at $E_x = 9.51$ MeV in ^{15}O. In particular, the s- and d-wave angular-momentum channels are separated.
Conclusion: The relative cross sections provide a consistent set of data that can be used to better constrain a full multichannel R-matrix extrapolation of the capture data. It has been demonstrated how the scattering data reduce the uncertainty through a preliminary Monte Carlo uncertainty analysis, but several other issues remain that make large contributions to the uncertainty, which must be addressed by further capture and lifetime measurements.

DOI: 10.1103/PhysRevC.91.045804 PACS number(s): 26.20.−f, 26.65.+t, 21.10.Tg

I. INTRODUCTION

Hydrogen burning in stars more massive than our sun is dominated by the CNO cycles. The least efficient reaction determines the overall rate of the cycle, and for the CN cycle, this reaction is ^{14}N(p,γ)^{15}O. This makes its reaction rate at stellar temperatures the most critical nuclear physics input parameter for modeling the cycle.

Recent solar neutrino measurements have reached unprecedented levels of sensitivity, obtaining measurements of the ^{8}B, ^{7}Be, and pp neutrino fluxes to 3% [1], 5% [2], and 11% [3] overall uncertainties, respectively. With the capability of precision flux measurements and a firm theoretical understanding of weak interactions, precision solar neutrino measurements stand ready to test the limitations of the standard solar model (SSM) [4]. In particular, these measurements provide a new and independent tool for determining the solar metallicity of our sun through measurements of the CNO neutrino fluxes. It has been estimated that the Sudbury Neutrino Observatory + (SNO+) can measure the flux of ^{15}O neutrinos with an

*rdeboer1@nd.edu
†Present address: Department of Physics and Astronomy, University of Tennessee Knoxville, Knoxville, Tennessee 37996, USA.
‡Present address: Department of Physics and Astronomy, Texas A, and M University, College Station, Texas 77843, USA.
§Present address: NASA George C. Marshall Space Flight Center, Huntsville, Alabama 35812, USA.

uncertainty level of 7% with three years of running [4]. On the SSM side, the largest source of uncertainty is the cross section of ^{14}N$(p,\gamma)^{15}$O, which has been estimated at 7% [5]. The ^{14}N$(p,\gamma)^{15}$O reaction is also an important input parameter in models that determine the age of globular clusters and correspondingly the age of the universe (see, e.g., Ref. [6]).

As with many reactions of interest in stellar burning scenarios, the extremely small cross sections at stellar energies, a result of the Coulomb repulsion of the two entrance channel nuclei, makes a direct measurement impossible with current techniques. The cross section at the energies of interest must thus be obtained through an extrapolation of the higher energy data combined with a detailed knowledge of the level properties of the compound nucleus and the different reaction components. The cross section is often determined by fitting the experimental data by using a phenomenological R matrix [7,8]. The reaction framework provides the energy and angular dependence of resonance transitions, but requires experimental data to constrain the specific properties of the levels. The more complicated the level structure, the more data are required to obtain a unique and confident solution. Therefore, it is often critical to fit all open channels of a reaction simultaneously [9]. If the data sets are found to be consistent, this gives more confidence in the phenomenological description and decreases both the systematic and statistical uncertainty in the extrapolation.

For the low energies of interest, only the ground-state proton and γ-ray channels are open for ^{14}N $+ p$ reactions (see Fig. 1). While the ^{14}N$(p,\gamma)^{15}$O reaction has been studied several times, the S factor at solar energies remains uncertain to at least 7% [5]. In addition, the uncertainty is enhanced by conflicting extrapolations near the low energy resonance at $E_{\text{c.m.}} = 259$ keV [10,11]. The scattering cross section has also been studied many times, but here there are even more inconsistencies in the data [12,13].

The level structure of ^{15}O near the proton separation energy is reasonably well established, but several specific properties remain uncertain or ambiguous, which can affect the extrapolation of the ^{14}N$(p,\gamma)^{15}$O cross section to zero energy. Chief among these are the γ-decay width of the $E_x = 6.79$ MeV subthreshold state [$\Gamma_\gamma = 0.41^{+34}_{-13}$ eV (90% C.L.) [14], 0.95^{+60}_{-95} eV [15], >0.85 eV [16]], the absolute strength (≈5% uncertainty) of the low energy resonance at $E_{\text{c.m.}} = 259$ keV, and contributions of broad higher energy resonances tailing into the low energy range. Of the seven possible γ-ray transitions to bound states in ^{15}O, three are estimated to account for ≈90% of the total cross section at stellar energies, with the ground-state transition accounting for between 15% and 30% of the total [5,10,11]. This transition is especially difficult to extrapolate because the $E_x = 6.79$ MeV subthreshold state strongly interferes with other resonances and with the direct capture process, as shown in Fig. 2. Asymptotic normalization coefficients (ANCs) have been measured for the $E_x = 6.79$ MeV state and others [17,18] as a way to constrain the contributions from direct capture and the tail of the 6.79 MeV state. However, the large uncertainty in the 6.79 MeV state's γ width implies that the ANC alone does not provide a significant constraint on the contribution of the subthreshold state.

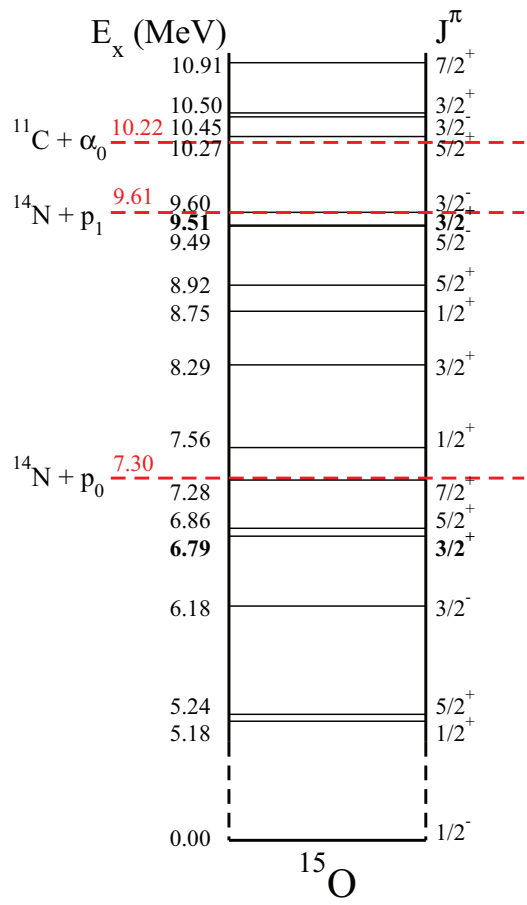

FIG. 1. (Color online) Level diagram of the ^{15}O nucleus. While the highest energy data are above both the p_1 and α separation energies, decay probabilities to these channels are neglected. States of special interest for the present study are marked in bold at $E_x = 6.79$ and 9.51 MeV. Several narrow resonances ($\Gamma_{\text{total}} < 1$ keV) are ignored because they have a negligible effect on the fitting of the excitation curves and on the extrapolation of the capture cross section to stellar energies.

The $E_{\text{c.m.}} = 259$ keV resonance, corresponding to the lowest energy unbound state in ^{15}O, has been studied directly by Refs. [10,11,19]. These measurements strongly constrain this level's properties but the strength of the resonance remains uncertain to about 5%. Because the $J^\pi = 3/2^+ E_x = 6.79$ MeV subthreshold state has such a strong high energy tail, other broad $3/2^+$ unbound states interfere with it to produce the complicated interference observed at low energies. The most significant of these interfering states is the broad resonance at $E_{\text{c.m.}} = 2.21$ MeV, which corresponds to the level at $E_x = 9.51$ MeV, but higher energy states may also contribute. The partial widths of this broad resonance remain uncertain ($\Gamma_p \approx 200$ keV, $\Gamma_{\gamma_0} = 9.1\,(20)$ eV [20]).

Measurements of the ^{14}N$(p,p)^{14}$N reaction can provide important constraints on the reaction mechanism. In this paper, we report on a new measurement of ^{14}N$(p,p)^{14}$N over a wide angular range and in the energy range of interest for the ^{14}N$(p,\gamma)^{15}$O reaction. Although several previous elastic scattering experiments are reported in the literature, their

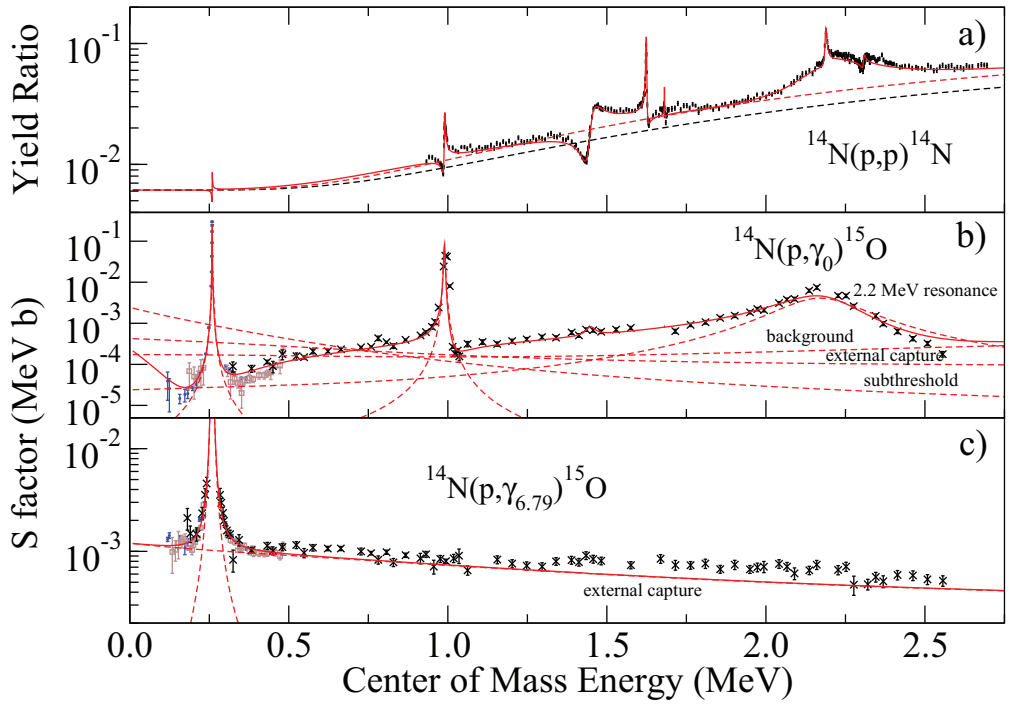

FIG. 2. (Color online) Example simultaneous R-matrix fits to elastic scattering (this work), ground-state, and 6.79 MeV capture data [11] (solid blue), [10] (brown open squares), [19] (black crosses), illustrating the connection of the 6.79 MeV ANC to each channel, the complexity of the ground state, and the relative simplicity of the 6.79 MeV primary transition. Throughout the figure the solid red line represents the R-matrix fit, which has been performed on the three channels simultaneously. Panel (a) shows an example of the scattering data yield ratios reported in this work ($\frac{d\sigma/d\Omega_{160^\circ}}{d\sigma/d\Omega_{30^\circ}}$). The black dashed line represents pure hard-sphere Coulomb scattering with angular momentum truncated at $l = 7$. The red dashed line represents the Coulomb scattering and the 6.79 MeV subthreshold state. Panel (b) shows the fit to the ground-state capture data. The low energy region is a complicated mixture of the contributions from the low energy tail of the $3/2^+$ $E_{\text{c.m.}} = 2.21$ MeV resonance, background contributions from higher-lying $3/2^+$ resonances, ground-state external capture, and the 6.79 MeV subthreshold state. Panel (c) shows the capture to the 6.79 MeV state where the cross section is dominated by external capture and the single narrow resonance at $E_{\text{c.m.}} = 259$ keV.

results are often inconsistent, yielding differences in absolute-cross-section scales, energy calibration, and sometimes even energy dependence [12,13]. Part of these discrepancies may be the result of poor target stability since solid nitrogen compounds used for transmission targets are often unstable under long-term bombardment, making the extraction of absolute cross sections very challenging. A substantial amount of the target effects are avoided by analyzing the relative yields of the measurements instead. This technique has proved very useful for the R-matrix analysis of the $^{12}\text{C} + \alpha$ reactions [21].

In Sec. II the details of the experiments are presented. This is followed by a description of the extraction of the yield ratios and the R-matrix analysis in Sec. III. A discussion of the data is given in Sec. IV and a summary is given in Sec. V.

II. EXPERIMENT AND RESULTS

Two complementary experimental setups were employed for the measurements. The first setup utilized an accelerator that could reach low energies and used a windowless gas target, which provided a nearly-contaminant-free background but only allowed for measurements at a few angles. The second setup allowed for detailed angular distributions but was constrained by an accelerator that could not reach as low in energy. Additionally, the solid self-supporting target had impurity peaks arising from the backing material and the solid nitrogen compound that was used.

The first measurements were made over a low energy range from $E_p = 1.0$ to 3.0 MeV. The proton beam was supplied by the 4 MV KN Van de Graaff accelerator at the University of Notre Dame's Nuclear Science Laboratory (NSL). Beam currents were of the order of a few hundred nA. The energy calibration of the Van de Graaff was established to better than 1 keV by using the well known $^{27}\text{Al}(p,\gamma)^{28}\text{Si}$ resonance at 0.992 MeV [22]. For this setup the windowless gas-target system RHINOCEROS [23] was used. This gas target has been used extensively in the past and is very well characterized (see, e.g., Refs. [24,25] and references therein). Nitrogen gas, depleted in ^{15}N and kept at a pressure of $\sim$0.25 Torr, was used throughout the experiment. This corresponds to a target thickness of $\approx$0.5 μg/cm^2. The target chamber was very similar to the one shown in Fig. 2(a) of Ref. [25], except that additional view ports were available at $\theta_{\text{lab}} = 135^\circ$, 150°, and 165°. Ruggedized silicon photodiode detectors were mounted at $\theta_{\text{lab}} = 30^\circ$, 90°, 105°, 135°, 150, and 165° approximately 6 cm from the center of the gas target. The uncertainty in the laboratory angle is estimated to be 0.5° based on the uncertainty in the geometry. Because of the high-purity target,

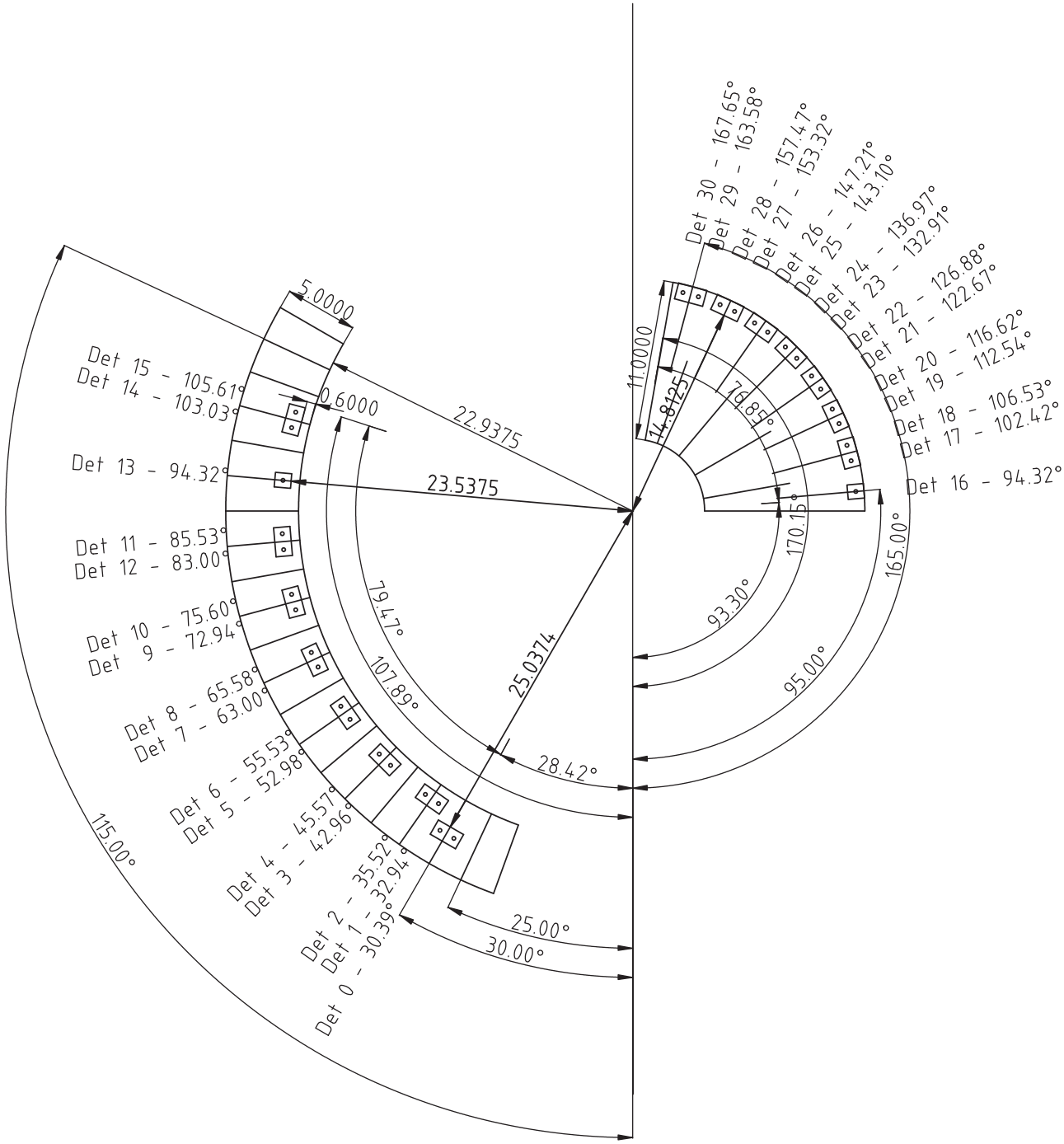

FIG. 3. Schematic of the detection setup for the higher energy solid-target measurements.

no contaminant peaks were observed, giving very clean yield spectra.

For the second measurement, a proton beam of energy from $E_p = 1.8$ to 4.0 MeV was supplied by the 10 MV FN Tandem Van de Graaff accelerator at the NSL. The accelerator's energy calibration was verified to ≈2 keV by using well-known narrow resonances in the $^{12}C(\alpha,\alpha)^{12}C$ reaction [21]. The target was an ≈20 μg/cm^2-thick layer of Adenine ($C_5H_5N_5$) of natural isotopic abundance evaporated on a carbon backing foil, also of natural abundance and of similar thickness. The target was mounted at 35° relative to the horizontal beam axis on an electrically isolated target ladder. The angle was chosen to minimize energy straggling of the scattered particles and to prevent the target ladder from blocking the line of sight to any of the detectors. Beam currents were kept below 300 nA in an effort to avoid rapid target degradation. A 76-cm-radius (30-inch-radius) scattering chamber housed the detector array. The scattering chamber contains a rotating table for detector mounting and alignment. By using a fixed telescope and the rotating table, the detector angles were found

to be reproducible to 0.1°. The table is equipped with fixed mounting positions for the detectors, allowing for accurate reproducibility of the detector-to-target distance. The radial distance of the detectors to the target were determined to 0.1 cm. Because the geometric setup is critical for the analysis, uniformity of the detector setup was checked by comparing with Rutherford scattering from gold at $E_\alpha = 6.575$ MeV, placing a mixed α source at the target position, and by comparing ^{12}C(α,α)^{12}C angular distributions with those of Ref. [26]. The overall setup is very similar to that described in Ref. [21] and a schematic diagram is shown in Fig. 3.

The detector array consisted of 28 1 cm × 1 cm Hamamatsu photodiodes. The detectors were mounted with 0.625(6) cm (1/4 inch) diameter collimators. The uniformity of the collimator sizes were determined to be within 1.1% by making measurements using a fixed geometric setup and a radioactive α source. The detectors were placed 37.6 (1) cm from the target at backward angles and at 59.8 (1) cm at forward angles. The difference in distance helped to mitigate the high count rate at very forward angles. Two detectors were placed symmetrically across the beam axis at $\theta_{\rm lab} = 94.3°$ in order to monitor the effect of changes in the position of the beam spot on the target. The detectors had an energy resolution of ≈20 keV, allowing for separation of the scattering peaks from the contaminant reactions. Observed contaminant peaks were from ^{12}C and ^{13}C in the natural isotopic backing and target material and ^{16}O absorbed in the backing.

Because of the limited resolution of the silicon detectors, the scattering peaks from ^{14}N could not always be separated from the ^{12}C, ^{13}C, and ^{16}O peaks depending on the incoming proton beam energy and detector angle. Of critical importance for the analysis is that the ^{14}N scattering peak can always be separated from the contaminant peaks at the most backward angle of $\theta_{\rm lab} = 167.7°$. This was observed to be possible down to the lowest energy of $E_p = 1.8$ MeV. For each run a background run was also measured by using a blank carbon foil backing of similar thickness.

The Adenine-target material has a relatively low melting point of 360° C. Over the course of the experiment the target was monitored by repeatedly scanning over the narrow ^{14}N(p,p)^{14}N resonance at $E_p = 3.19$ MeV ($\Gamma = 3\,(1)$ keV) [20]. No change in the peak position was observed from carbon buildup, but the yield decreased substantially. About 50% of the initial target material was lost over the course of the experiment.

III. ANALYSIS

Because of past problems with absolute-cross-section measurements, this analysis extracts the ratio of the experimental yields. For reactions with strong anisotropic resonance transitions, differential yield ratios can provide strong constraints on the level parameters when analyzed in a reaction framework like R matrix (see, e.g., Ref. [21]). Furthermore, the target thickness approximately cancels in the yield ratio, greatly reducing what is often one of the largest sources of systematic uncertainty. While not as critical for the current measurement, the integrated charge can also be difficult to measure accurately, especially if higher-Z beam particles are used. The remaining uncertainties, when the reaction peaks are cleanly separable, are then largely from statistics and from geometric quantities; for example, the solid angles of the detectors, which can usually be measured to high precision.

Given the good approximation that the change in the differential cross section as a function of energy is small compared to the energy loss of the beam particles through the target material, thin-target approximations can be used in the analysis. The effective energy of the beam was calculated by using the approximation $E_{\rm eff} = E_p - \Delta E/2$, where ΔE is the energy loss through the thin target. The differential yield observed for a given reaction peak in the energy spectrum is given approximately by

$$dY \approx N_b N_t \epsilon \left(\frac{d\sigma}{d\Omega}\right) d\Omega, \tag{1}$$

where N_b is the total number of beam particles incident on the target, N_t is the number of active target atoms per unit area, ϵ is the efficiency, and $d\Omega$ is the solid angle subtended by an individual detector. Since several detectors were employed, each differential yield was measured simultaneously. As a result, N_b and N_t are the same for each angle at a given energy. Then the ratio of the yields at angle 1 to angle 2 is

$$\begin{aligned}\frac{dY_1}{dY_2} &\approx \frac{N_b N_t\,(d\sigma/d\Omega)_1\,d\Omega_1\epsilon_1}{N_b N_t\,(d\sigma/d\Omega)_2\,d\Omega_2\epsilon_2} \\ &\approx \frac{(d\sigma/d\Omega)_1}{(d\sigma/d\Omega)_2}\frac{d\Omega_1\epsilon_1}{d\Omega_2\epsilon_2}.\end{aligned} \tag{2}$$

Because the detector efficiencies and solid angles have all been determined, the cross section ratios can be extracted.

For the gas-target setup, the pure ^{14}N gas ensured that the spectra had very little background and the extraction of the yields was straightforward. A forward detector at $\theta_{\rm lab} = 30°$ was used as the normalization detector. The ratio of the yields of the other detectors relative to this one is shown in Fig. 4.

For the solid-target setup, the extraction of the ^{14}N yields was complicated by the presence of the contaminant peaks from ^{12}C, ^{13}C, and ^{16}O. For each run a background run was also performed using a blank carbon backing that contained all of the contaminant nuclei observed in approximately the same stoichiometry. The main contaminant peak was ^{12}C, which often had a yield several times that of the ^{14}N peak. The ^{13}C and ^{16}O peaks were only small contaminants, estimated to be less than 2% of the yield of the ^{14}N peak over the entire energy range.

The relative ^{14}N yields were extracted by using two different techniques. If the ^{14}N peak could be clearly separated from the other scattering peaks, its yield was extracted directly. This was often the case for backward angle detectors (i.e., $\theta_{\rm lab} > 90°$). If the ^{14}N peak and a contaminant peak overlapped, a subtraction method was used. For each of the runs at each energy, the background run was first normalized to the Adenine-target run by using the ^{12}C peak yields in the most backward angle detector ($\theta_{\rm lab} = 167.65°$) where all of the scattering peaks were always resolvable, as demonstrated in Fig. 5. The spectra at each angle were then subtracted from each other in order to obtain the ^{14}N yield. The ^{14}N yield, determined through either method, was then divided by the ^{14}N yield of the

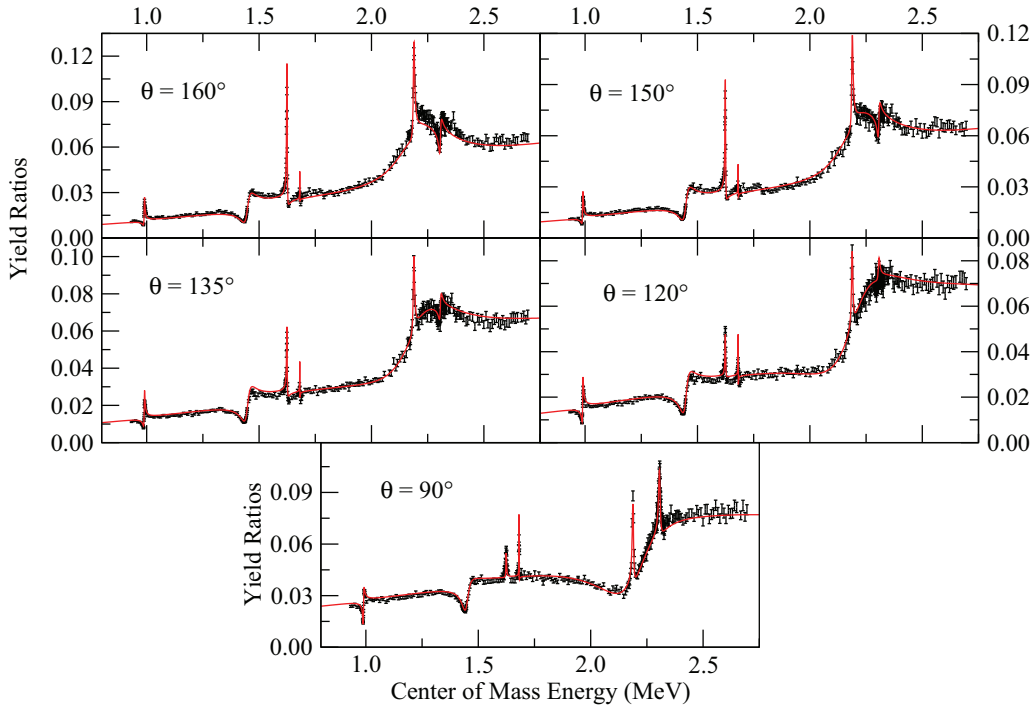

FIG. 4. (Color online) Yield ratios of the ^{14}N$(p,p)^{14}$N reaction measured by using a gas-target setup. The reference angle is $\theta_{\rm lab} = 30^\circ$. Uncertainties are statistical only. The solid red line indicates the R-matrix fit.

most-backward-angle detector to obtain the relative yields. To check the consistency of the method, the background subtraction was implemented even when the peaks could be separated. A comparison of the yield ratios resulting from the two techniques is shown in Fig. 6.

To monitor the effect of the beam-spot position on the target, two detectors were placed at the same angle, $\theta_{\rm lab} = 94.32^\circ$, but on opposite sides of the target, as shown in Fig. 7. The yield ratios were found to be in good agreement indicating that

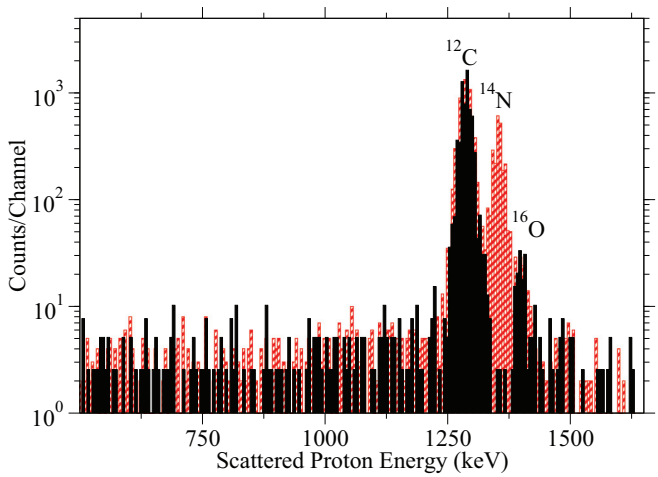

FIG. 5. (Color online) Spectra for the lowest beam energy (E_p = 1.8 MeV) at the most backward angle ($\theta_{\rm lab} = 167.7^\circ$). The red hashed histogram represents the Adenine run and the black filled histogram represents the background run with a carbon foil only. The spectra have been normalized to each other by using the areas of the carbon peaks.

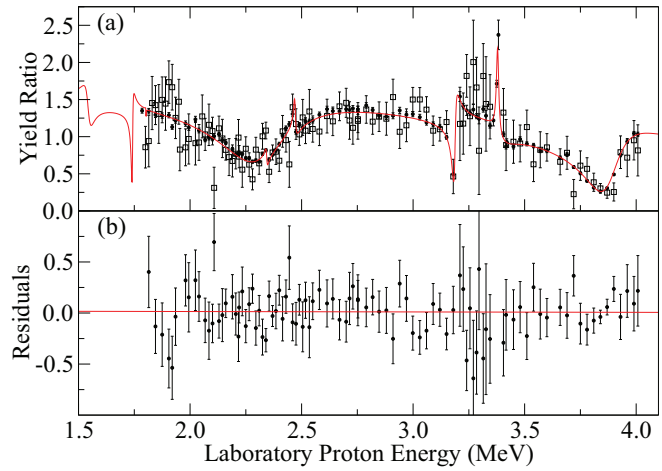

FIG. 6. (Color online) Panel (a) shows a comparison of the yield ratio at $\theta_{\rm lab} = 112.5^\circ$ to the most-backward-angle detector at $\theta_{\rm lab} = 165.7^\circ$ obtained for separately resolved ^{14}N and ^{12}C scattering peaks (black circles) to when the background-subtraction method is used (open squares). The red solid line represents the R-matrix fit, which is shown to guide the eye. In panel (b) the difference between the separately resolved peak yields and those from the subtraction method are shown. The expectation is that the average value should be zero. A linear fit was performed that resulted in $\Delta y = -0.004E_p + 0.023$ with $\chi^2 = 79.7$ (97 data points). Setting the slope and intercept parameters to zero yields a χ^2 of 80.1 and a corresponding $\Delta\chi^2 = 0.4$, within 1σ uncertainty ($\Delta\chi^2 < 1$).

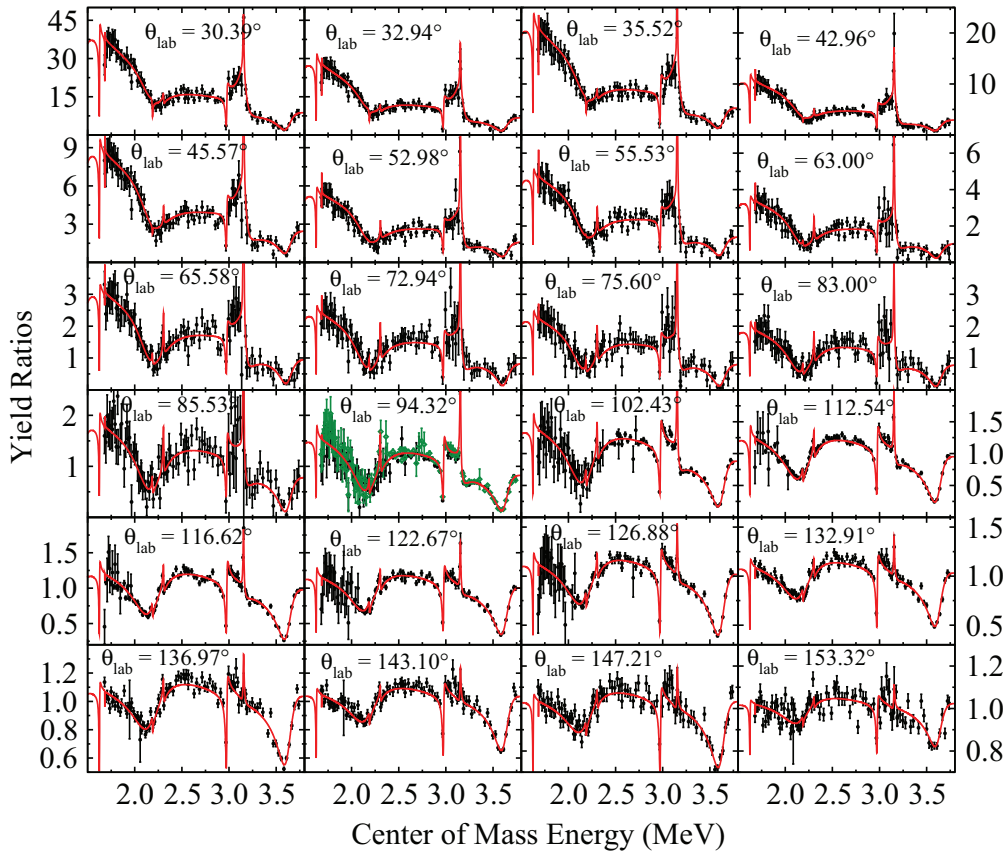

FIG. 7. (Color online) Yield ratios of the ^{14}N$(p,p)^{14}$N reaction measured by using a solid-target setup. The reference angle is $\theta_{\rm lab} = 167.65^{\circ}$. Uncertainties are statistical only. The solid red line indicates the R-matrix fit. The yield ratio curve at $\theta_{\rm lab} = 94.32^{\circ}$ compares the results from the two detectors at the same angle but on opposite sides of the beam, as denoted by the black circular points and green diamond points for the closer distance of 37.6 (1) cm and the farther distance of 59.8 (1) cm, respectively.

effects from changes in the beam-spot position were negligible compared to the statistical uncertainties.

The differential cross sections and yield ratios are fit simultaneously in an R-matrix framework using the code AZURE2 [27]. The analysis used a channel radius of 4.2 fm and a maximum orbital angular momentum of $l = 7$. The parametrization of Ref. [28] has been used so that widths from the literature may be used as starting parameters for the fit. Starting values for the level parameters (J^{π}, E, Γ_p) have been taken from the compilation [20]. Figure 1 shows the levels that were considered in the analysis. Narrow resonances have been neglected. Figures 4 and 7 show the fits to the data from the gas-target measurement and from the solid-target setup, respectively. The fits were performed to all the data simultaneously. Table I lists the final values of the level parameters from the R-matrix fit.

Because of the quantity of data, the statistical uncertainties of the derived level parameters are usually quite small. Even though the statistical uncertainties from the solid-target measurements are rather large on a point-to-point basis, owing to the background subtraction, this is compensated by the many angles of measurement. The statistical uncertainties were calculated by using the routine MINOS, available as part of MINUIT2 analysis package [29]. Uncertainties at a 1σ level were determined by using a value of $\Delta\chi^2 = \sqrt{\chi^2/N}$ [30] where the best fit yielded a value of $\chi^2_{\rm min}/N = 2.34$ for 4614 data points. The systematic uncertainties on the energies come chiefly from the uncertainty in beam energy, the target thickness, and the R-matrix model. The uncertainties in energy and target thickness are approximately constant over the range of each of the experimental measurements while the model uncertainties vary depending on the resonance. For the partial widths of the resonances, the model uncertainties from the R-matrix analysis often dominate. The full listing of all the uncertainties considered is given in Table I.

The uncertainties in the parameters are also sensitive to the value of the adopted channel radius. An initial channel radius of 5.5 fm was used, based on similar radii that were adopted for the analysis of ^{14}N$(p,\gamma)^{15}$O data (see, e.g., Refs. [9–11,31]). A preliminary fit was obtained by using a value of 5.5 fm but subsequent sensitivity studies found that the fit preferred a smaller channel radius of 4.2 fm. Furthermore, compared to the value of $\Delta\chi^2$ adopted for the rest of the uncertainty analysis a range of only 4.2 ± 0.1 fm was found to be within this range. It is interesting to note that this smaller value of the channel radius is consistent with the one obtained in Ref. [5] (4.14 fm) for the best fit to the $E_x = 6.79$ MeV transition. The uncertainty in the level parameters arising from this range of radius can be quite significant and is reflected in the model uncertainties listed in Table I.

TABLE I. Level parameters extracted from the R-matrix fit to the scattering data. A channel radius of 4.2 fm was used and the parametrization of Ref. [28] is used to fit physical parameters directly. Partial widths are given in the center-of-mass frame. Energies of subthreshold states were fixed at the values given in the compilation [20], and ANCs are fixed to those given in Ref. [17] after changing from an (l,j) to an (s,l) coupling scheme. Uncertainties are of the form (statistical, systematic, model). Fitted parameters are given in bold font. In some cases multiple channels are allowed for the same l. In most cases only one of these channels was necessary, hence some possible channels are omitted.

	E_x (MeV)				Γ (keV) or ANC (fm$^{-1/2}$)	
J^π	This work	Literature	l	s	This work	Literature
$\frac{1}{2}^-$	0		1	0.5		0.23 (1)
$\frac{1}{2}^-$			1	1.5		7.4 (4)
$\frac{1}{2}^-$	15		1	0.5	**4.2(10,40,1)$\times 10^3$**	
$\frac{1}{2}^-$			1	1.5	**5.5(20,10,5)$\times 10^3$**	
$\frac{1}{2}^+$		5.183 (1)	0	0.5		0.33 (6)
$\frac{1}{2}^+$		7.5565 (4)	0	0.5		0.99 (10)
$\frac{1}{2}^+$	**8.7501 (3,10,3)**	8.743 (6)	0	0.5	**37.1 (2,8,2)**	32
$\frac{1}{2}^+$	15		0	0.5	**7.3 (16,38,7)$\times 10^3$**	
$\frac{3}{2}^-$		6.1763 (17)	1	0.5		0.47 (3)
$\frac{3}{2}^-$			1	1.5		0.53 (3)
$\frac{3}{2}^-$	**9.6041 (2,10,1)**	9.609 (2)	1	0.5	**0.87 (3,3,1)**	8.8 (5)
$\frac{3}{2}^-$			1	1.5	**10.6 (4,4,1)**	
$\frac{3}{2}^-$	**10.4519 (8,20,26)**	10.48	1	0.5	**16.5 (7,39,1)**	25 (5)
$\frac{3}{2}^-$			1	1.5	**1.8 (6,7,1)**	
$\frac{3}{2}^-$	15		1	0.5	**0.40 (2,1,16)$\times 10^3$**	
$\frac{3}{2}^-$			1	1.5	**2.5 (2,1,3)$\times 10^3$**	
$\frac{3}{2}^+$		6.7931 (17)	0	1.5		4.9 (5)
$\frac{3}{2}^+$	**8.2866 (2,10,1)**	8.2840 (5)	0	1.5	**2.93 (2,6,0)**	3.6 (7)
$\frac{3}{2}^+$			2	1.5	**0.91 (3,10,1)**	
$\frac{3}{2}^+$	**9.5061 (11,10,12)**	9.484 (8)	2	0.5	**114.2 (9,6,2)**	$\approx$200
$\frac{3}{2}^+$			0	1.5	**158.7 (11,11,14)**	
$\frac{3}{2}^+$	**10.4971 (21,20,16)**	10.506	2	0.5	**25.0 (14,82,10)**	140 (40)
$\frac{3}{2}^+$			0	1.5	**121 (3,1,3)**	
$\frac{3}{2}^+$	13		2	0.5	**830 (110,240,80)**	
$\frac{3}{2}^+$			0	1.5	**3.51 (6,310,16)$\times 10^3$**	
$\frac{3}{2}^+$			2	1.5	**4.89 (14,460,70)$\times 10^3$**	
$\frac{5}{2}^-$	**9.4852 (2,10,1)**	9.488 (3)	1	1.5	**7.3 (2,10,0)**	10.1 (5)
$\frac{5}{2}^-$	15		1	1.5	**4.0 (2,6,3)$\times 10^3$**	
$\frac{5}{2}^+$		5.2409 (3)	2	0.5		0.23
$\frac{5}{2}^+$			2	1.5		0.24
$\frac{5}{2}^+$		6.8594 (9)	2	0.5		0.39 (2)
$\frac{5}{2}^+$			2	1.5		0.42 (2)
$\frac{5}{2}^+$	**8.9214 (2,10,0)**	8.922 (2)	2	1.5	**3.20 (3,30,1)**	3.3 (3)
$\frac{5}{2}^+$	**10.2691 (5,20,2)**	10.3	2	1.5	**8.2 (3,0,1)**	11 (2)
$\frac{5}{2}^+$	15		2	0.5	**5.0 (2,3,0)$\times 10^3$**	
$\frac{7}{2}^+$		7.2759 (6)	2	1.5		1541 (59)
$\frac{7}{2}^+$	**10.9063 (8,20,6)**	10.917 (12)	2	1.5	**85.1 (7,2,6)**	90

IV. DISCUSSION

Several resonances are observed over the proton bombarding energy range from $E_{\text{c.m.}} = 0.90$ to 3.75 MeV. This analysis concentrates on the broad resonance structures that may have an effect on the extrapolation of the $^{14}\text{N}(p,\gamma)^{15}\text{O}$ cross section to astrophysical energies, especially for the ground-state transition. Of particular interest is the broad resonance at $E_{\text{c.m.}} = 2.21$ MeV, which corresponds to the

$3/2^+$ level at $E_x = 9.51$ MeV in ^{15}O and the branching of its width into $l = 0$ and 2 channels. The importance of this level and its branching has been highlighted in Refs. [9,19,31], for example. This level can be populated through three possible channels depending on the coupling of the channel spin (s) and orbital angular momentum (l): $(s,l) = (\frac{3}{2},0)$, $(\frac{1}{2},2)$, and $(\frac{3}{2},2)$. The R-matrix fit finds that both $l = 0$ and 2 channels are required. A good fit can be obtained using only the $(\frac{3}{2},0)$ and $(\frac{1}{2},2)$ channels, but since the angular distributions for the two $l = 2$ channels are similar, only the sum of their widths can be determined accurately. The uncertainty analysis results in a much-improved estimate of the total proton width for this state and the branching between $l = 0$ and 2 (see Table I).

To achieve the R-matrix fit shown in Figs. 4 and 7, a number of background poles were required to simulate the low energy tails of higher energy resonances. For the most part, these background poles are only needed to fit the data above $E_{\text{c.m.}} = 3$ MeV. In particular, they are needed to fit the high energy side of the $E_{\text{c.m.}} = 2.21$ MeV ($J^\pi = 3/2^+$, $E_x = 9.51$ MeV) resonance and the highest energy data near the resonance at $E_{\text{c.m.}} = 3.60$ MeV ($J^\pi = 7/2^+$, $E_x = 10.91$ MeV). The quality of the fit was insensitive to the exact energy of all but the $3/2^+$ background pole. The reduced widths of the $3/2^+$ background pole were quite sensitive to its energy. In this regard, it is useful to compare the reduced widths from the fits with the corresponding Wigner limits (see, e.g., Ref. [32]). When the $3/2^+$ background pole was placed at $E_x = 15$ MeV, the fit resulted in values for the partial width that were much larger than the Wigner limit. If the pole was instead placed at a lower energy, the fitted widths were greatly reduced. Therefore, for the final fit, the $3/2^+$ background pole was placed at $E_x = 13$ MeV. This sensitivity of the placement of the background pole suggests that there is a real broad $3/2^+$ level(s) at energies just above the data. Indeed, Ref. [20] reports broad levels ($\Gamma \approx 1$ MeV) given tentative spin assignments of $(1/2,\ 3/2)^+$ at $E_x = 13.45$ and 15.10 MeV. This is also consistent with R-matrix fits to the ground-state capture data, which require a significant contribution from a $3/2^+$ background pole (see Fig. 2).

To determine the branchings between channels of the same angular momentum but different intrinsic spin with greater sensitivity, polarization experiments could be performed but the number of observables that would likely need to be measured, the complexity of the analysis, and the lack of a low energy polarized beam facility makes this unlikely in the near future.

While the inelastic proton channel is also open at the highest energies ($E_{\text{c.m.}} > 2.3$ MeV), inclusion of this channel in the calculations did not increase the quality of the fit. Inelastic protons were only observed in the experimental data at $E_{\text{c.m.}} > 3.5$ MeV, confirming the small branching to this channel.

A preliminary multichannel R-matrix fit has been performed in order to illustrate the constraint of the scattering data on the capture data. Example data for the scattering channel (this work), ground-state γ-ray channel, and $E_x = 6.79$ MeV γ-ray channel [10,11,19] are shown in Fig. 2 and were fit simultaneously. The $^{14}\text{N} + p$ reactions represent a clear example of how the ANC can affect different reaction channels

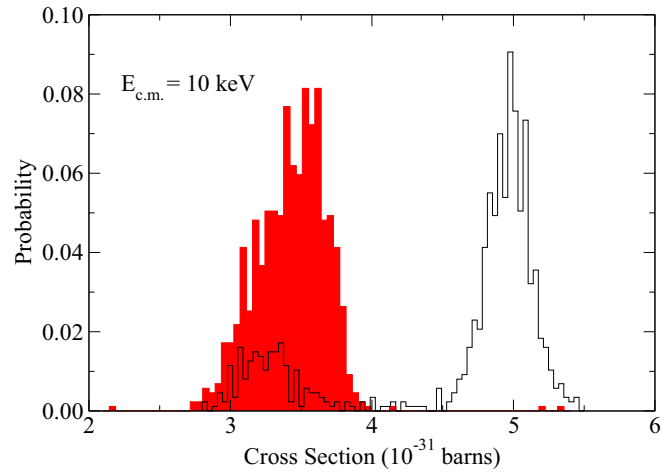

FIG. 8. (Color online) Example probability densities for the $^{14}\text{N}(p,\gamma)^{15}\text{O}$ ground-state transition cross section obtained from Monte Carlo uncertainty analyses. The black outlined unfilled histogram represents the result obtained when only the capture data from Refs. [10,11,19] were considered. The red solid histogram results when the scattering data of this work is also included.

either as a subthreshold state (scattering or ground-state γ-ray channel) or as the strength of the external capture ($E_x = 6.79$ MeV γ-ray channel). The implementation of the ANC in R-matrix theory, to describe both of these reaction components, is given in detail in Ref. [33]. In Fig. 2(a) it is shown how the $E_x = 6.79$ MeV subthreshold state makes a strong contribution to the scattering channel. While the scattering data cannot constrain the value of the ANCs as strongly as the transfer reactions, the measurements should be consistent, as is the case here. Furthermore, by demonstrating that a simultaneous fit is achievable gives more confidence in the applicability of the phenomenological model.

An extrapolation of the S factor for the ground-state transition is shown in Fig. 2(b). This preliminary fit was performed by considering fixed normalizations for each of the data sets and is quite similar to that presented in Ref. [5] except with the inclusion of scattering data. To demonstrate the effect that the scattering data has on the fit, the uncertainty was first calculated by using only the capture data. This was done by using a Monte Carlo technique similar to that described in Ref. [34], except only point-to-point uncertainties were considered. As shown in Fig. 8 by the black outlined unfilled histogram, a bimodal probability density was produced corresponding to the tension between the energy dependence and normalizations of the different capture data sets. The red filled histogram shows the probability density resulting from the same fit but with the scattering data of this work also included. The probability density is now constrained to a single peak that overlays the lower cross section peak of the calculation with out the scattering data. It is rather interesting to note that, in the original calculation, the higher cross section solution was significantly more probable.

While this demonstrates the significance of the scattering data, other uncertainties, like the sensitivity of the fit to the channel radius, background poles, experimental systematic uncertainties, and compatibility of the different capture data

sets, are very significant and must be characterized before a new recommended value of the low energy S factor can be given. To accomplish this, a detailed global analysis is in progress, which also includes newly measured capture data that cover the higher energy range [35]. These new capture data have been measured with the aim of improving on those of Ref. [19], where important summing corrections were neglected, as discussed in Refs. [5,11].

V. SUMMARY

While several measurements exist for the $^{14}\mathrm{N}(p,p)^{14}\mathrm{N}$ reaction, they are often inconsistent and many lack detailed uncertainties. A consistent set of yield ratio scattering data has been measured over the energy range $0.9 < E_{\mathrm{c.m.}} < 3.75$ MeV. The data strongly constrain the proton partial widths of resonances that contribute to the astrophysically important $^{14}\mathrm{N}(p,\gamma)^{15}\mathrm{O}$ reaction, in particular the broad $3/2^+$ resonance at $E_{\mathrm{c.m.}} = 2.21$ MeV. A preliminary multichannel R-matrix fit illustrates how the subthreshold states affect the scattering and capture data, mainly the $E_x = 6.79$ MeV state. A preliminary uncertainty analysis demonstrates how the inclusion of the scattering data leads to a more confident extrapolation of the ground-state capture cross section. However, other uncertainty contributions remain, which are of equal or greater significance, that must be addressed through further capture and lifetime measurements.

ACKNOWLEDGMENTS

This research was supported in part by the Notre Dame Center for Research Computing and funded by the National Science Foundation through Grant No. PHY-1068192, the Joint Institute for Nuclear Astrophysics Grant No. PHY08-22648, and in part by the US Department of Energy under Contract No. DE-FG02-97ER41041.

[1] SNO Collaboration, B. Aharmim *et al.*, Phys. Rev. C **81**, 055504 (2010).
[2] Borexino Collaboration, G. Bellini *et al.*, Phys. Rev. Lett. **107**, 141302 (2011).
[3] Borexino Collaboration, Nature (London) **512**, 383 (2014).
[4] W. Haxton, R. Hamish Robertson, and A. M. Serenelli, Annu. Rev. Astron. Astrophys. **51**, 21 (2013).
[5] E. G. Adelberger *et al.*, Rev. Mod. Phys. **83**, 195 (2011).
[6] L. M. Krauss and B. Chaboyer, Science **299**, 65 (2003).
[7] A. M. Lane and R. G. Thomas, Rev. Mod. Phys. **30**, 257 (1958).
[8] P. Descouvemont and D. Baye, Rep. Prog. Phys. **73**, 036301 (2010).
[9] R. E. Azuma *et al.*, Phys. Rev. C **81**, 045805 (2010).
[10] R. C. Runkle, A. E. Champagne, C. Angulo, C. Fox, C. Iliadis, R. Longland, and J. Pollanen, Phys. Rev. Lett. **94**, 082503 (2005).
[11] G. Imbriani *et al.*, Eur. Phys. J. A **25**, 455 (2005).
[12] P. F. Bertone, Ph.D. thesis, The University of North Carolina at Chapel Hill, 2010 (upublished).
[13] A. Gurbich, Nucl. Instrum. Methods Phys. Res., Sect. B **266**, 1193 (2008).
[14] D. Schürmann, R. Kunz, I. Lingner, C. Rolfs, F. Schümann, F. Strieder, and H.-P. Trautvetter, Phys. Rev. C **77**, 055803 (2008).
[15] K. Yamada *et al.*, Phys. Lett. B **579**, 265 (2004).
[16] P. F. Bertone, A. E. Champagne, D. C. Powell, C. Iliadis, S. E. Hale, and V. Y. Hansper, Phys. Rev. Lett. **87**, 152501 (2001).
[17] A. M. Mukhamedzhanov *et al.*, Phys. Rev. C **67**, 065804 (2003).
[18] P. F. Bertone, A. E. Champagne, M. Boswell, C. Iliadis, S. E. Hale, V. Y. Hansper, and D. C. Powell, Phys. Rev. C **66**, 055804 (2002).
[19] U. Schröder, H. Becker, G. Bogaert, J. Görres, C. Rolfs, H. Trautvetter, R. Azuma, C. Campbell, J. King, and J. Vise, Nucl. Phys. A **467**, 240 (1987).
[20] F. Ajzenberg-Selove, Nucl. Phys. A **523**, 1 (1991).
[21] P. Tischhauser *et al.*, Phys. Rev. C **79**, 055803 (2009).
[22] J. Keinonen and A. Anttila, Comment. Physico-Math. **46**, 61 (1976).
[23] J. Hammer, W. Biermayer, T. Griegel, H. Knee, and K. Petkau, *RHINOCEROS, the Versatile Stuttgart Gas Target Facility (Part I)* (unpublished).
[24] M. Jaeger, R. Kunz, A. Mayer, J. W. Hammer, G. Staudt, K. L. Kratz, and B. Pfeiffer, Phys. Rev. Lett. **87**, 202501 (2001).
[25] K. Wolke, V. Harms, H. W. Becker, J. W. Hammer, K. L. Kratz, C. Rolfs, U. Schröder, H. P. Trautvetter, M. Wiescher, and A. Wöhr, Z. Phys. A **334**, 491 (1989).
[26] R. J. deBoer, A. Couture, R. Detwiler, J. Görres, P. Tischhauser, E. Uberseder, C. Ugalde, E. Stech, M. Wiescher, and R. E. Azuma, Phys. Rev. C **85**, 045804 (2012).
[27] ASURE2 R-matrix code.
[28] C. R. Brune, Phys. Rev. C **66**, 044611 (2002).
[29] F. James and M. Roos, Comput. Phys. Commun. **10**, 343 (1975).
[30] W. Press, S. Teukolsky, W. Vetterling, and B. Flannery, *Numerical Recipies: The Art of Scientific Computing*, 3rd ed. (Cambridge University Press, New York, 2007).
[31] C. Angulo and P. Descouvemont, Nucl. Phys. A **690**, 755 (2001).
[32] C. E. Rolfs and W. S. Rodney, *Cauldrons in the Cosmos*, 1st ed. (The University of Chicago Press, Chicago, 1988).
[33] A. M. Mukhamedzhanov and R. E. Tribble, Phys. Rev. C **59**, 3418 (1999).
[34] R. J. deBoer, J. Görres, K. Smith, E. Uberseder, M. Wiescher, A. Kontos, G. Imbriani, A. Di Leva, and F. Strieder, Phys. Rev. C **90**, 035804 (2014).
[35] Q. Li, J. Görres, R. J. deBoer, G. Imbriani, A. Best, A. Kontos, P. J. LeBlanc, E. Uberseder, and M. Wiescher (unpublished).